Geophysical Journal International

Geophys. J. Int. (2012) **188,** 1117–1128 doi: 10.1111/j.1365-246X.2011.05299.x

Combining seismic arrays to image the high-frequency characteristics of large earthquakes

Eric Kiser and Miaki Ishii

Department of Earth & Planetary Sciences, Harvard University, 20 *Oxford Street, Cambridge, MA* 02138*, USA. E-mail: kiser@fas.harvard.edu*

Accepted 2011 November 14. Received 2011 November 12; in original form 2011 May 5

SUMMARY

This study investigates the source properties of the 2007 M_w 8.0 Pisco, Peru, 2007 M_w 8.4 and 7.9 Mentawai Islands, Indonesia, 2009 M_w 8.1 Samoa Islands and 2010 M_w 8.8 Maule, Chile, earthquakes using a backprojection technique that utilizes data from multiple seismic arrays. Combining seismic arrays increases azimuth and distance coverage and improves lateral resolution. The four subduction interface events show rupture propagation towards the bottom of the seismogenic zone. In addition, all of the earthquakes show evidence of multiple rupture segments with varying rupture speeds and directions. Relating these segments to the specific features of the subduction zones (e.g. interseismic coupling) suggests that asperity sizes may be controlled by subtle features of the subducted slab.

Key words: Earthquake dynamics; Earthquake source observations; Seismicity and tectonics; Subduction zone processes.

1 INTRODUCTION

One of the most important roles of seismology is characterizing the complexity of large earthquakes. Shortly after a large event, estimates of rupture parameters such as regions of highest slip, rupture speed and rupture direction all contribute to assessing potential hazards, such as the generation of tsunamis and the intensity of ground shaking. In addition, it has been argued that large earthquakes are controlled by topographic features of the subducting plate and coupling along the subduction interface (e.g. von Huene *et al.* 1997; Moreno *et al.* 2010). For such comparisons to be made, an accurate description of the source complexity is needed. We approach this problem by applying a backprojection technique to determine the spatio-temporal behaviour of energy release for the 2007 M_w 8.0 Pisco, 2007 M_w 8.4 & 7.9 Mentawai Islands, 2009 M_w 8.1 Samoa Islands and 2010 M_w 8.8 Maule earthquakes. In contrast to a traditional slip inversion, which requires important parameters such as fault orientation and rupture velocity to be specified *a priori*, the backprojection method requires little *a priori* information. This implies that complexities of rupture patterns are less likely to be obscured by initial assumptions.

Though methods which utilize the time-reversal property of seismic waves have been around for almost 25 years (e.g. McMechan *et al.* 1985; Rietbrock & Scherbaum 1994; Ekström *et al.* 2003; Kao & Shan 2004, 2007; Baker *et al.* 2005; Krüeger & Ohrnberger 2005; MacAyeal *et al.* 2006), the backprojection method, using dense network data with empirical corrections, was first applied to the 2004 Sumatra-Andaman earthquake by Ishii *et al.* (2005). The rupture of this giant event, as imaged using backprojection, had a length of nearly 1300 km and lasted almost 600 s. This study showed the capability of the backprojection method, and has resulted in subsequent source studies that utilize the technique (e.g. Ishii *et al.* 2007; Walker *et al.* 2005; Allmann & Shearer 2007; Nelson *et al.* 2008; Honda & Shin 2009; Walker & Shearer 2009; Xu *et al.* 2009; Lay *et al.* 2010a,b,c; Kiser & Ishii 2011; Kiser *et al.* 2011; Meng *et al.* 2011). Though these studies have provided important insights into the rupture parameters of both large and small earthquakes, problems with artefacts and poor lateral resolution still limit the method's applicability. In this study, we attempt to address these issues by combining backprojection results from multiple arrays at different distances and azimuths. In addition to revealing rupture details of five subduction zone earthquakes, this study will present synthetic tests that demonstrate the usefulness of different arrays for monitoring a given subduction zone.

2 METHOD

The backprojection technique uses the curvature of wave fronts recorded at large aperture, dense seismic arrays and the time-reversal property of these waves to determine their source location. This is achieved by time-shifting and stacking seismograms to a grid of potential source locations around the hypocentre (e.g. Ishii *et al.* 2007). The time-shifts are based upon the theoretical travel-times from each seismic station to each potential gridpoint using a 1-D velocity model such as IASP91 (Kennett & Engdahl 1991). The potential source gridpoints can be set up in three dimensions (i.e. latitude, longitude and depth), but we focus on the laterally varying behaviour of giant earthquakes in this study by fixing the depth at the hypocentral depth. This constant depth assumption is reasonable because the depth extent of energy release for large, shallow earthquakes is difficult to constrain using teleseismic data (Kiser *et al.*

2011). Therefore, using a dipping plane of gridpoints to simulate the orientation of a rupture plane (e.g. the plate interface) has little effect on the backprojection results.

The stacks at each gridpoint, $s_i(t)$, take the form

$$s_i(t) = \sum_{k=1}^{K} \alpha_k \, u_k \, (t - t_{ik} + \Delta t_k) \, , \tag{1}$$

where $u_k(t)$ is the seismogram recorded at the kth station, t_{ik} is the predicted traveltime between gridpoint i and station k, Δt_k is the station-specific time correction, α_k is the station-specific weighting factor and K is the total number of seismograms. The 1-D earth model, with which t_{ik} is calculated, does not include lateral variations that can produce deviations in the arrival times of seismic waves. To correct for these lateral variations, the initial few seconds of the P waveforms are cross-correlated (Ishii *et al.* 2007). The cross-correlation provides the time-shift Δt_k that is required to align the waveforms coherently at the hypocentre. The alignment of waveforms at the hypocentre means that the energy distribution is imaged with respect to this point. Therefore, if a different hypocentre is used, the backprojection results will be shifted by the changes in the hypocentral location. This dependence on the hypocentre can change the interpretation of backprojection results in terms of the surrounding tectonic environment.

The cross-correlation also provides relative amplitude and polarity information for each seismogram that can be used to normalize the contribution from each station to the stack $s_i(t)$. This normalization factor takes the form

$$\alpha_k = \frac{p_k}{A_k},$$

where p_k corrects for polarity changes within the seismic array and has a value of either 1 or -1. A_k is an amplitude factor for seismogram k. Using this weighting scheme ensures that a small group of high-amplitude seismograms do not dominate the final stacks.

The modification made to the backprojection technique to incorporate multiple seismic arrays is similar to the modification made in Kiser *et al.* (2011) to combine multiple seismic phases recorded at the same array. At each gridpoint, stacked seismograms are generated for the jth array, $s_{ji}(t)$, using eq. (1). The stacks from different arrays are then combined at each gridpoint giving the final stacks, $S_i(t)$ in the form

$$S_i(t) = \sum_{j=1}^{J} w_j \, | \, s_{ji}(t + \Delta t_j) |,$$

where J is the number of seismic arrays being considered, w_j is the array-specific weighting factor, and Δt_j is the array-specific time correction. The weighting factor and time correction act to normalize individual array contributions and enhance coherence, respectively. The weighting factor takes the form

$$w_j = \frac{A_{\mathrm{ref}}^{\mathrm{max}}}{A_j^{\mathrm{max}}},$$

where $A_{\mathrm{ref}}^{\mathrm{max}}$ is the maximum absolute amplitude of the reference seismic array stack at the hypocentre, and A_j^{max} is the maximum absolute amplitude of the hypocentral stack of the jth seismic array. To ensure that stacks from different arrays combine coherently, the absolute values of the hypocentral stacks from different arrays are cross-correlated against the absolute values of the hypocentral reference stack. The resulting time-shift, Δt_j, is applied to all of the stacks from the jth seismic array.

3 DATA AND DATA PROCESSING

In this study, we use two seismic arrays, the High Sensitivity Seismograph Network (Hi-net) in Japan and the USArray Transportable Array (TA) in the United States. Hi-net, which began reporting data in 2000 October, currently has around 800 stations with a targeted station spacing of 20 km. Borehole short-period instruments (100 samples per second) with all three components are placed typically at 100 m depth (e.g. Okada *et al.* 2004; Obara *et al.* 2005). In contrast, TA consists of 400 high-quality three-component broad-band seismometers with a targeted station spacing of 70 km (http://www.usarray.org/researchers/obs/transportable). This temporary array stretches from the northern to the southern border of the continental United States. It was first deployed in the west coast states in 2007 August, and has been moving eastwards since then. Only the vertical components in these arrays are used in this study, and data from both arrays are bandpass filtered between 1 and 5 Hz, with 1 s period waves dominating the signal.

As described in Section 2, there are two time corrections applied to these data, one to correct for lateral variations in the the velocity structure of the Earth (Δt_k) and one to ensure that the hypocentral stacks add coherently from different arrays (Δt_j). Within each array, we cross-correlate each seismogram with a reference seismogram as outlined in Ishii *et al.* (2007) to obtain the time-shift Δt_k. Δt_j is obtained by cross-correlating the hypocentral stacks from TA and Hi-net. For all five earthquakes, the TA stacks are used as the reference stacks.

In addition to these two time corrections, there are also two weighting factors α_k and w_j. The station-specific weighting factor, α_k, normalizes the seismograms within each array, and is obtained from the same cross-correlation procedure that determines Δt_k. The array-specific weighting factor, w_j, is the ratio of the maximum amplitudes of the hypocentral stacks from each array. Fig. 1 shows an example of the hypocentral stacks from the Samoa Islands event after these time corrections and weighting factors have been applied.

This study investigates the 2007 M_{w} 8.0 Pisco, Peru, 2007 M_{w} 8.4 Mentawai Islands, 2007 M_{w} 7.9 Mentawai Islands, 2009 M_{w} 8.1 Samoa Islands and 2010 M_{w} 8.8 Maule, Chile, earthquakes. Four of these events have epicentres relative to Hi-net or TA that require us to use seismic phases other than the direct P phase, which is typically used in backprojection studies (e.g. Ishii *et al.* 2005, 2007; Walker *et al.* 2005; Walker & Shearer 2009). For the 2007 Peru event, the range of distances from the hypocentre to Hi-net is 133°–150°, hence there is a core phase triplication (e.g. *PKPab*, *PKPbc* and *PKIKP*; Fig. 2). Based upon visual inspection of the seismograms, we find that using the stations with distances at or greater than 146° isolates a coherent *PKPbc* arrival, and this is the phase used in the

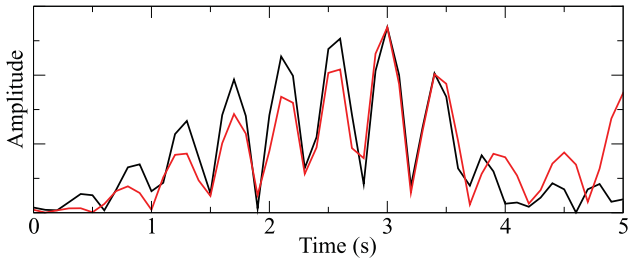

Figure 1. Combining stacks. Backprojection stacks from TA (red) and Hi-net (black) at the epicentre of the 2009 Samoa Islands earthquake after the time correction Δt_j and weighting factor w_j are applied. Time is with respect to the epicentral time.

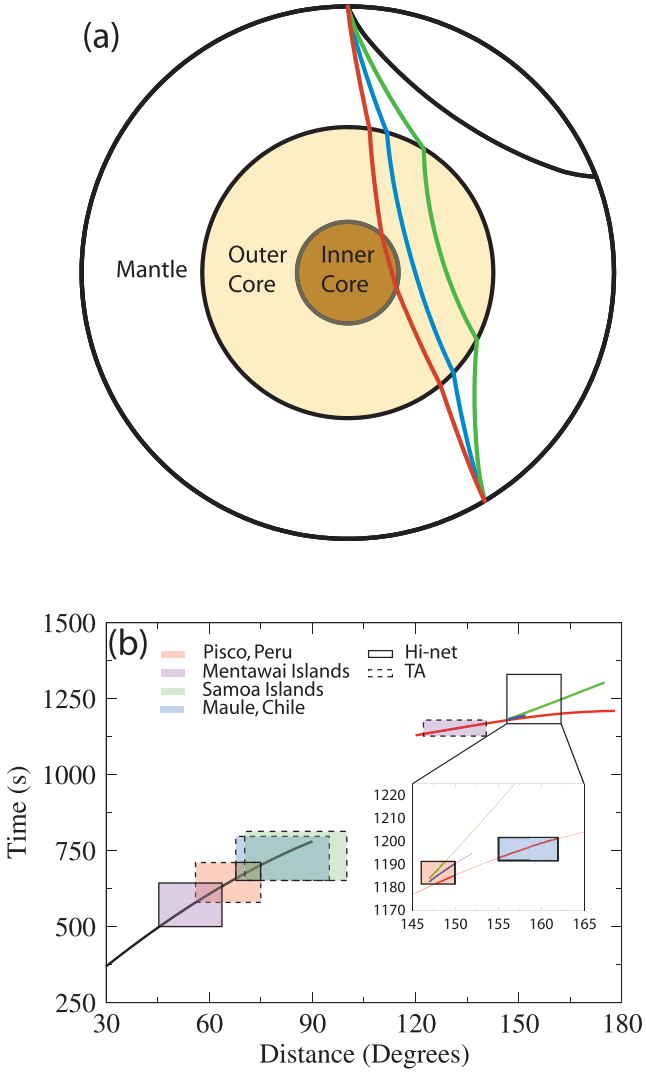

Figure 2. Ray paths. (a) Ray paths for the *P* (black), *PKPab* (green), *PKPbc* (blue) and *PKIKP* (red) seismic phases. (b) Traveltime plot for the *P* (black), *PKPab* (green), *PKPbc* (blue) and *PKIKP* (red) seismic phases. The inset shows the core phase triplication. The rectangles show the distance ranges of TA and Hi-net from the four regions studied.

backprojection analysis. Limiting the distance of the stations for this specific earthquake reduces the number of seismograms to 137. The range of distances of Hi-net stations from the hypocentre of the 2010 Chile event is 150°–162°. Limiting the stations used to distances of 155° and greater results in a set of 367 seismograms with coherent *PKIKP* phase arrivals. The hypocentres of the two 2007 Mentawai Islands earthquakes are at distances between 121° and 141° from TA such that the *PKIKP* phase is the first to arrive. No distance constraint is applied to the TA data for either of the Mentawai Islands events.

4 RESULTS AND DISCUSSION

For each of the five events studied, we estimate the rupture duration, rupture direction, rupture length, rupture speed and the spatial distribution of energy release for the entire rupture. The rupture duration is estimated from the relative source–time function of the backprojection results. For the total duration, we choose the end of the rupture to correspond to the time at which the amplitude from the relative source–time function lowers to a value between 0.3 and 0.4 of the maximum value. This means that the estimates of total duration are probably lower bounds, since it can be argued that the end of the rupture occurs at the time when the amplitude is the same as at the hypocentral time (typically around 0.1 of the maximum amplitude). Rupture direction, rupture length and rupture speed are calculated based upon the centres of the energy kernels at different times during the rupture. Earthquake subevents are identified based upon dramatic changes in rupture direction and speed. For the earthquakes with multiple subevents, rupture duration, rupture direction, rupture length and rupture speed are given for each subevent. To determine the spatial distribution of energy release for the entire earthquake, we select a contour that encloses an area that matches the moment magnitude given by the USGS earthquake catalogue assuming a typical stress drop of 30 bars (Kanamori 1977; http://earthquake.usgs.gov/earthquakes/). The results of each earthquake are followed by a comparison of the rupture parameters with those from previous studies. In addition, we discuss the results in the context of rupture segmentation and the seismogenic zone.

4.1 The 2007 August 15 M_w 8.0 Pisco, Peru, earthquake

Fig. 3(a) shows the distribution of energy release for the entire Pisco, Peru, earthquake. This result indicates that the rupture is very compact. The relative source–time function shows that there are two distinct subevents with durations of 20 s each (Fig. 3b). The first subevent propagates southeast from the epicentre at a speed of about 1.3 km s^{-1}, with a total rupture length of 25 km (Fig. 3c). The second subevent starts slightly updip of the terminus of the first subevent, and has a larger amplitude of relative energy release than the first event. This rupture propagates north at a speed of 2.5 km s^{-1}, and has a rupture length of 50 km (Fig. 3c). The spatial gap between the terminus of the first subevent and the beginning of the second subevent is about 15 km to the west and the temporal gap is about 25 s.

Numerous studies using seismic and geodetic data have investigated the rupture of the 2007 Peru event (e.g. Motagh *et al.* 2008; Pritchard & Fielding 2008; Biggs *et al.* 2009; Hébert *et al.* 2009; Lay *et al.* 2010a; Perfettini *et al.* 2010; Sladen *et al.* 2010). Most of these results have largest slip west or southwest of the Paracas Peninsula, with only minor moment release near the epicentre. The backprojection results showing low-amplitude energy release near the epicentre (subevent 1) agree well with these previous studies. In addition, the high amplitude of the second subevent imaged by the backprojection analysis, and its updip location with respect to the epicentre are consistent with previous work (Fritz *et al.* 2008; Motagh *et al.* 2008; Pritchard & Fielding 2008; Biggs *et al.* 2009; Hébert *et al.* 2009; Sladen *et al.* 2010). However, in contrast to most studies which place this second rupture west or southwest of the Paracas Peninsula, the rupture imaged by backprojection is located north of the Paracas Peninsula. One possible explanation for the discrepancy comes from the fact that we are using high-frequency data (1–5 Hz). The slip south of the Paracas Peninsula may have a longer rise time, and may not efficiently radiate high-frequency energy (e.g. Madariaga 1977). A longer rise time is also consistent with efficient excitation of tsunami waves from this region. In addition to differences in the general locations, the second rupture, as imaged by backprojection, propagates north, back towards the epicentre, at a velocity significantly higher than the initial

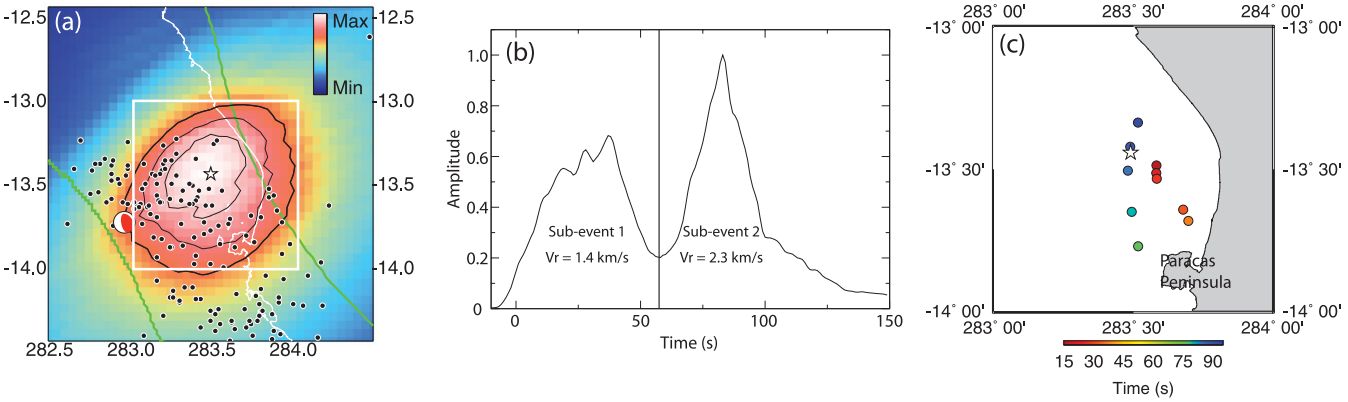

Figure 3. The 2007 August 15 Pisco, Peru, earthquake. (a) Spatial distribution of the normalized energy released during this earthquake as imaged by the backprojection method. This figure is obtained by integrating the squared amplitude of the stacks over a time window of 15 s. The light grey lines are the contours of maximum energy release in 10 per cent intervals. The focal mechanism is taken from the Global CMT Catalogue (Dziewonski *et al.* 1981; Dziewonski & Woodhouse 1983; http://www.globalcmt.org/). The epicentre (white star) and aftershock locations for the first 3 months following the main shock (black circles) come from the National Earthquake Information Center (http://earthquake.usgs.gov/earthquakes/). The thick black contour is the 70 per cent contour that represents the total rupture area for this event. The green lines are the upper and lower bounds of the seismogenic zone (Heuret *et al.* 2011). The white box is the region of (c). (b) Relative source–time function of the 2007 Peru event. The amplitude has been normalized so that the maximum amplitude is one. Time is with respect to the hypocentral time. (c) Locations (circles) of the imaged energy at different times during the rupture. The first subevent occurs between 15 and 35 s after the hypocentral time. The second subevent occurs between 75 and 95 s after the hypocentral time. For both subevents, the locations are plotted every 5 s. The white star is the epicentre. The times on the scale are with respect to the hypocentral time.

rupture. Both of the ruptures imaged using backprojection occur in a region of high interseismic coupling as determined using GPS data (Perfettini *et al.* 2010).

4.2 The 2007 September 12 M_w 8.4 and M_w 7.9 Mentawai Islands, West Sumatra, earthquakes

This pair of earthquakes takes place on 2007 September 12 in the Mentawai Islands region in Indonesia and is separated by 12 hr from each other. The energy distribution for the first event (M_w 8.4) is shown in Fig. 4(a). The backprojection result shows that most of the energy is released northwest of the epicentre. The relative source–time function shows a rupture duration of 90 s and energy is released continuously throughout the event, though there are two clear episodes of peak energy release (Fig. 4b). The rupture propagates mostly unilaterally to the northwest for about 170 km (Fig. 4c), which leads to an average rupture speed of 1.9 km s^{-1}. One interesting feature of the event is the downdip propagation at a latitude of about 4° south (Fig. 4c). This downdip propagation takes place 40 to 50 s after the epicentral time, and is followed by an increase in the along-strike rupture velocity from 1.4 to 2.5 km s^{-1}. The location of the downdip propagation also corresponds to a notable break in the aftershock distribution (Fig. 4c)

The second event (M_w 7.9) begins downdip of the terminus of the first event (Fig. 5a). The majority of the energy is released northwest and updip of the epicentre (Fig. 5a). The rupture is composed of two distinct high-amplitude subevents with durations of 30 and 40 s. These subevents are separated by 25 s of low-amplitude energy release, which leads to a total duration of 95 s (Fig. 5b). The along-strike length of the total rupture is about 150 km, leading to

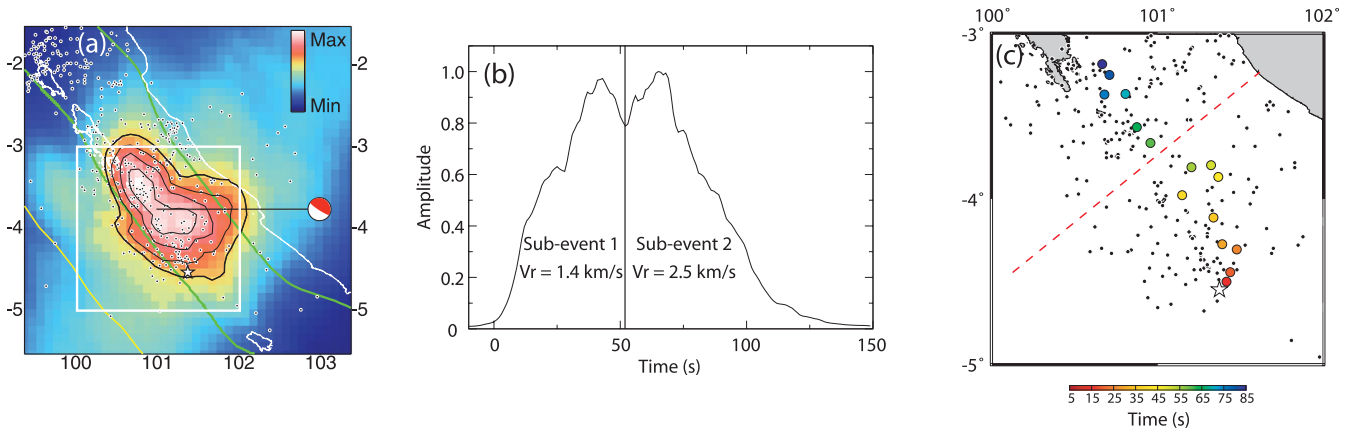

Figure 4. The 2007 September 12 M_w 8.4 Mentawai Islands earthquake. (a) The same as in Fig. 3(a) except that the thick black contour is the 60 per cent contour that represents the total rupture area for this event. The yellow line is the trench location. The CMT is offset from its location to show the changes in energy release better, and the black line connected to the CMT plot shows its actual location. (b) The same as Fig. 3(b) except for the 2007 M_w 8.4 Mentawai Islands event. (c) The same as Fig. 3(c). The red dashed line marks the break in the aftershocks for the first 3 months following the main shock. The coloured circles are plotted between 5 and 90 s after the hypocentral time every 5 s.

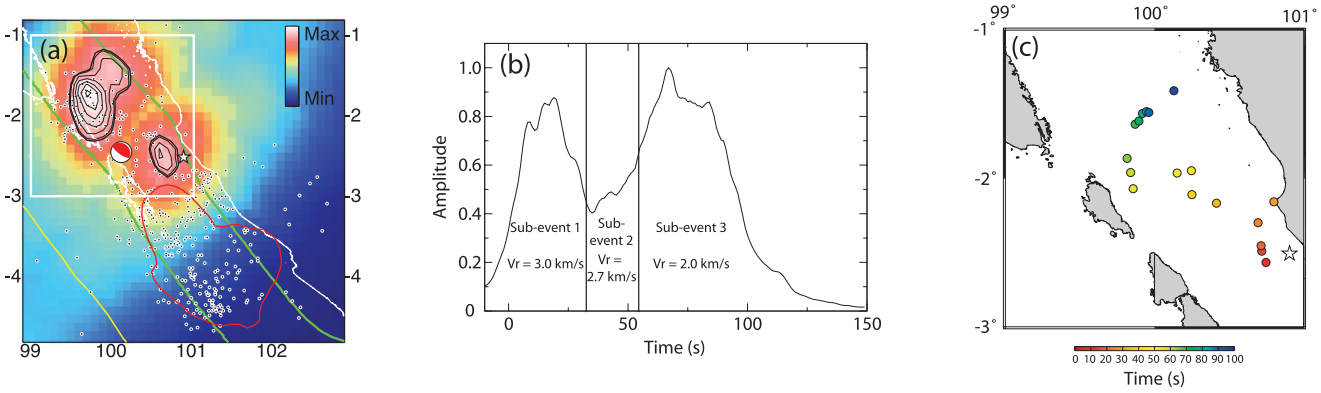

Figure 5. The 2007 September 12 M_w 7.9 Mentawai Islands earthquake. (a) The same as in Fig. 3(a) except that the thick black contour is the 83 per cent contour that represents the total rupture area for this event. The yellow line is the trench location, and the red contour is the 60 per cent contour of the M_w 8.4 event (Fig. 4a). (b) The same as Fig. 3(b). (c) The same as Fig. 3(c). The coloured circles are plotted between 5 and 90 s after the epicentral time every 5 s.

an average rupture speed of 1.6 km s^{-1}. The distribution of rupture locations has a distinct dumbbell shape showing that the main energy release had extensive propagation along the dip direction (Fig. 5c). Note that this along-dip rupture makes the above average rupture speed estimate of 1.6 km s^{-1} a lower bound. Between the two episodes of along-dip propagation, lower amplitude energy is seen to travel smoothly along strike. Dividing the rupture into three subevents provides a much more complete rupture picture. The first subevent propagates mainly downdip to the north/northeast for a distance of 45 km and at a speed of 3.0 km s^{-1}. The second, low-amplitude subevent propagates along-strike to the northwest for about 40 km at a velocity of 2.7 km s^{-1}. Finally, the third subevent propagates mostly downdip to the northeast at a velocity of 2.0 km s^{-1} for a distance of 80 km.

A previous study of the 2007 September 12 Mentawai Islands earthquakes agrees well with the backprojection results of this study. Using GPS, coral and InSAR data, Konca *et al.* (2008) determined a northwest trending distribution of slip away from the epicentre for both the 8.4 and 7.9 events. These results show a concentration of slip into two asperities for both events, consistent with results obtained in this study. In addition, Konca *et al.* (2008) also show extensive downdip rupture of the asperities of the 7.9 event.

The rupture patterns imaged by the backprojection analysis for both events correlate well with the pattern of interseismic coupling along the Sunda subduction zone, where the regions of highest coupling also experienced the highest energy release (Chlieh *et al.* 2008; Konca *et al.* 2008). The one exception to this conclusion is the first part of the M_w 8.4 event which takes place in a region of low coupling south of South Pagai Island, though the sparseness of GPS and coral data may make it difficult to determine the coupling in this region (Chlieh *et al.* 2008).

4.3 The 2009 September 29 M_w 8.1 Samoa Islands earthquake

Unlike the other events in this study, the 2009 Samoa Islands event is an intraplate event that occurred in the outer rise of the Tonga subduction zone. The energy release of this event is focused around the epicentre (Fig. 6a). However, the relative source–time function reveals significant complexity with at least two subevents composing the earthquake (Fig. 6b). The first, weak subevent begins at the epicentre and propagates north for around 15 s at an average speed of 1.8 km s^{-1}. The rupture length of this subevent is 25 km (Fig. 6c, Movie S1). The second subevent, which releases most of the energy, originates about 50 km northwest and 10 s after the terminus of the first subevent, and lasts 20 s with a rupture length of 40 km and a rupture velocity of 2.0 km s^{-1} to the southeast (Fig. 6c, Movie S1). The propagation velocity between the end of the first subevent and

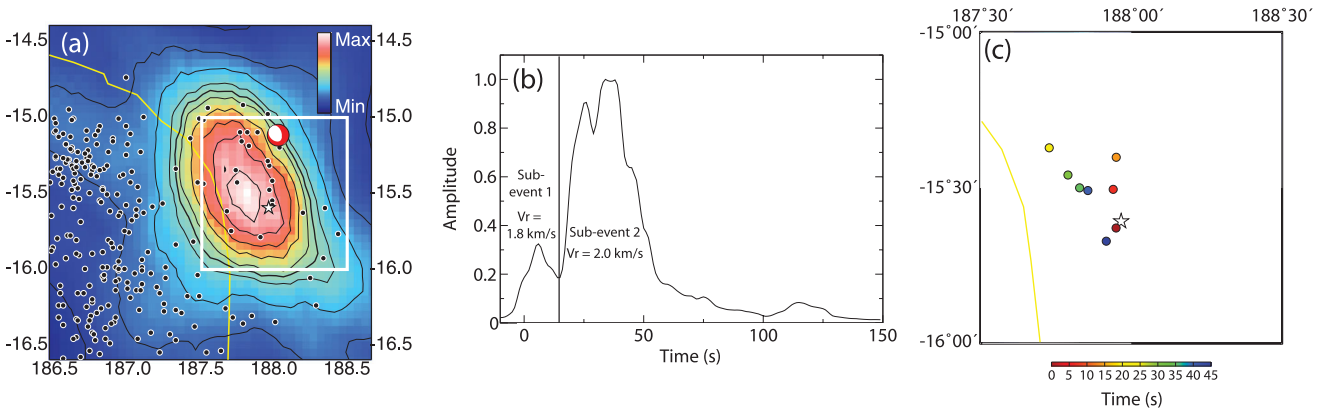

Figure 6. The 2009 September 29 Samoa Islands earthquake. (a) The same as in Fig. 3(a). This plot is made by integrating the squared amplitude of the stacks over a time window of 10 s. The thick black contour is the 45 per cent contour that represents the total rupture area for this event. (b) The same as Fig. 3(b) except for the 2007 M_w 8.1 Samoa Islands event. (c) The same as Fig. 3(c). The first subevent occurs between 0 and 14 s after the hypocentral time and the coloured circles are plotted every 7 s. The second subevent occurs between 25 and 45 s after the hypocentral time and locations are plotted every 5 s.

beginning of the second subevent is about 5.0 km s^{-1}. This is much higher than the *S*-wave speed at 10–20 km depth (3.4 km s^{-1} based upon IASP91; Kennett & Engdahl 1991).

The 2009 September 29 Samoa Islands earthquake has been modelled using seismic, GPS and tsunami data (Beavan *et al.* 2010; Lay *et al.* 2010c; Okal *et al.* 2010). Two of these studies argue for a 'hidden' thrust event in addition to the normal event in the outer rise (Beavan *et al.* 2010; Lay *et al.* 2010c). Using GPS and tsunami data, Beavan *et al.* (2010) prefer a model in which a thrust event with a long rise time (>200 s) occurs on the subduction interface and precedes the outer rise normal event by about 2 min. In this model, the moment magnitude of the thrust event is slightly larger than the outer rise event that follows. A second model that could not be ruled out by Beavan *et al.* (2010) is that the thrust event occurs shortly after (<50 s) the normal event and has a much shorter rise time than in the first model (<100 s). This model agrees with Lay *et al.* (2010c) who model the earthquake using both body and surface waves. Their preferred model has two smaller interface thrust events (M_w 7.8) occurring 50–90 s and 90–130 s after the initiation of the M_w 8.1 outer rise normal event. The activation of the subduction interface is corroborated by increased seismic activity (Fig. 6b). Most of the aftershocks occur west of the trench, and only a few aftershocks are located near the outer rise region.

In contrast to these studies, the backprojection results presented in this manuscript show no significant energy release west of the trench (Fig. 6a). The earthquake is composed of two subevents with very different rupture directions, but they are both located in the outer rise region. There are, however, low-amplitude features in our results that may correspond to the thrust events argued by Lay *et al.* (2010c). The largest of these low-amplitude features occurs 120 s after the epicentral time and almost 75 km west of the trench (Movie S1). This feature has the timing and location of an aftershock imaged in Lay *et al.* (2010c). The next largest feature in the backprojection energy occurs at about the same time as the thrust events in Lay *et al.* (2010c), that is, 80 s after event initiation. However, the location of this energy is east of the trench in the outer rise instead of along the subduction interface (Movie S1). This location offset of the thrust event is also evident in some of the supplementary backprojection results accompanying Lay *et al.* (2010c) in which seismic arrays other than F-net are used.

The exact location of the thrust event has important implications for future seismic hazards in the region. For example, if the thrust event did occur on the plate interface, a similar event in the near future may be unlikely. On the other hand, if the thrust event occurred in the outer rise, the aftershocks along the plate interface may be a sign of stress transfer from the outer rise to the plate interface which could lead to an interplate thrust event. Such a stress transfer has been documented south of the Samoa Islands region, along the Kermadec subduction zone. A similar increase in seismicity along the plate interface is observed after the magnitude 7.3 1974 July 2 outer rise event followed by a magnitude 8.0 thrust event on the plate interface on 1976 January 14 (Habermann & Wyss 1984).

4.4 The 2010 February 27 M_w 8.8 Maule, Chile, earthquake

As demonstrated through the resolution tests in the following section, the Hi-net data do not provide substantial improvements to lateral resolution in the Chile region. Furthermore, the Hi-net data are noisy due to the large distance from the hypocentre. While the rupture can be imaged using both arrays (see Movie S2), TA provides very good lateral resolution for this event, and therefore we will only use data from this array.

The spatial extent of this event indicates that most of the rupture takes place north of the epicentre (Fig. 7a). The relative source–time function suggests that the rupture is composed of at least two subevents (Fig. 7b). The first subevent propagates bilaterally, both southwest and northeast away from the epicentre, though the northern rupture has a much higher amplitude (Fig. 7c, Movie S3). The extent of this northern component of the rupture is 100 km, and it lasts about 45 s. This leads to an average rupture speed of 2.2 km s^{-1}. The second subevent, as defined by the source–time function, is composed of two separate subevents, one north of the epicentre and one south of the epicentre. The rupture north of the epicentre begins updip (about 75 km north/northwest) of, and shortly after (10 s) the northern terminus of the first subevent, and has the largest energy release of all the subevents (Fig. 7b, Movie S3). The spatio-temporal gap between these two subevents requires a propagation velocity of 7.5 km s^{-1}, only slightly below the *P*-wave speed at the hypocentral depth [8.0 km s^{-1} given by ASP91 (Kennett & Engdahl 1991)]. The northern rupture propagates north at an average speed of 2.9 km s^{-1} with an along-strike length of 175 km and a duration of 60 s (Fig. 7c, Movie S3). In contrast, the rupture south of the epicentre has a substantially lower amplitude than the northern subevent. This makes it difficult to image the southern rupture until about 70 s after

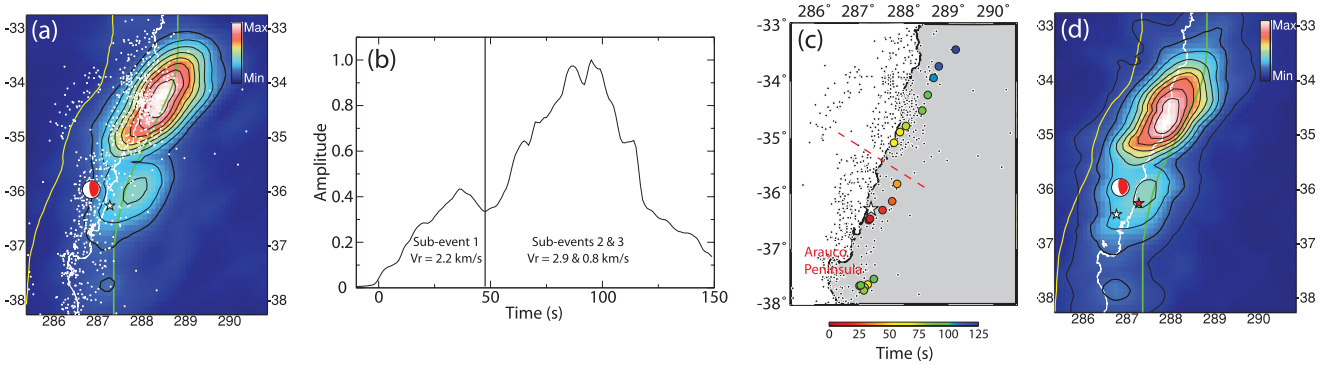

Figure 7. The 2010 February 27 Maule, Chile, earthquake. (a) The same as in Fig. 3(a). This plot is made by integrating the squared amplitude of the stacks over a time window of 20 s. The thick black contour is the 23 per cent contour that represents the total rupture area for this event. (b) The same as Fig. 3(b). (c) The same as Fig. 4(c) with the red dashed line showing a break in the aftershocks. (d) The same as (a) except using the hypocentre reported by the National Seismological Service in Chile. The white star is the epicentre reported by the National Seismological Service in Chile (36.47°S, 73.24°W) and the red star is the epicentre reported by NEIC.

rupture initiation at which time an episode of stronger energy release occurs. This rupture is either a continuation of the southward propagation of the initial rupture or it is a rupture on a separate fault segment. There is a significant reduction in the rupture velocity to 0.8 km s^{-1} and a change in the rupture direction to the east. This subevent lasts about 20 s, and has a length of 15 km (Fig. 7c, Movie S3).

Most of the previous studies of the M_w 8.8 2010 Maule, Chile, earthquake using seismic, geodetic and tsunami data generally agree with this study, with highest slip north of the epicentre (e.g. Delouis *et al.* 2010; Lay *et al.* 2010b; Moreno *et al.* 2010; Lorito *et al.* 2011). However, there have been conflicting reports regarding whether the high slip patches correlate with regions of high interseismic coupling (Moreno *et al.* 2010; Lorito *et al.* 2011). As with the Pisco, Peru and Mentawai Islands earthquakes, the two northern ruptures presented in this study correlate well with regions of high interseismic coupling, with the rupture jump occurring in a region of relatively low interseismic coupling (Moreno *et al.* 2010; Kiser & Ishii 2011).

4.5 Triggered slip on adjacent segments

Backprojection results from all five earthquakes show that these giant events are composed of multiple subevents. Evidence for this segmentation varies between subtle changes in rupture speed to abrupt changes in rupture direction. As reported in Sections 4.1–4.4, sometimes there is a notable jump in the rupture location accompanying the transition from one subevent to the next. In two cases, these jumps between the multiple ruptures occur where interseismic coupling along the subduction interface abruptly changes. For the 2010 Chile event, the jump occurs at about 35°S latitude where there is relative low coupling (Moreno *et al.* 2010). Similarly, the updip jump between the ruptures of the 2007 Pisco, Peru, event occurs at the edge of a high coupling zone, slightly north of where the Nazca Ridge subducts (Perfettini *et al.* 2010). These comparisons suggest that seismogenic segmentation of the slab interface is partially controlled by factors that dictate interseismic coupling. Furthermore, updip jumps are observed to accompany rupture segmentation. Given that rupture close to the trench has high potential for large tsunami excitation (e.g. Kanamori 1972), identifying regions where these updip jumps are likely to occur provides important information for defining regions that are most susceptible to tsunami hazard following large earthquakes.

In contrast to the interplate events, the 2009 Samoa Islands earthquake is an intraplate event that occurred in the outer rise of the Tonga subduction zone. In addition to our results, recent studies that relocated aftershocks of large outer rise events suggest that the rupture of multiple faults during large, outer rise earthquakes are a common occurrence (e.g. Fromm *et al.* 2006; Hino *et al.* 2009). One explanation for this behaviour comes from the fact that the lengths of outer rise faults are very similar, and normally fall between 5 and 30 km as observed from bathymetry data (e.g. Masson 1991). These observations suggest that there is a mechanism that limits the length of outer rise faults, which would also limit the size of earthquakes that can occur on any one of these faults. Therefore, to generate a large outer rise event, rupture on multiple faults may be necessary.

4.6 High-frequency energy and the seismogenic zone

There are interesting spatial relationships between the rupture distributions obtained using backprojection and the seismogenic zone. Figs 3(a), 4(a), 5(a) and 7(a) show that the majority of the imaged energy occurs within the seismogenic zones as determined from past seismicity in the different regions (Heuret *et al.* 2011). In fact, within the along-strike range of the ruptures, almost the entire seismogenic zone is covered during three of the four interplate events (Figs 3a, 4a and 5a). The one exception is the 2010 Maule, Chile, earthquake which has substantial energy downdip of the bottom of the seismogenic zone. This may be a real feature of the rupture, however, it should also be noted that there are large variations in the hypocentral locations reported for this earthquake. Because backprojection results are relative to the assumed hypocentral location, using a different hypocentre causes a translation of the imaged energy. For example, the hypocentre reported by the National Earthquake Information Center is used in Figs 7(a) and (c). However, the hypocentre reported by the National Seismological Service in Chile is significantly west of the NEIC location. Using the shifted hypocentre, the backprojection results also move west, and the energy release is almost entirely updip of the bottom of the seismogenic zone, which is more consistent with the observations from other large earthquakes (Fig. 7d).

For both of the 2007 Mentawai Islands earthquakes and the 2010 Chile earthquake, the transition from one rupture segment to the next occurs directly after the rupture approaches the downdip limit of the seismogenic zone. This downdip rupture propagation is somewhat surprising given that it has been argued that updip rupture propagation is common for both continental and subduction zone earthquakes (e.g. Sibson 1982; Kato & Seno 2003). However, since the bottom of the seismogenic zone is probably a region of high shear stress (e.g. Kato & Seno 2003), if a rupture initiates away from this zone, it does not seem unreasonable that the rupture would propagate into this region. The discrepancy between this result and previous studies may be caused by the fact that we are using high-frequency data, as opposed to aftershock distributions or lower frequency data typically used in finite-fault modelling.

5 SYNTHETIC TESTS

Backprojection results show a large degree of complexity during large earthquakes. In this section we explore the robustness of the complexity by providing and discussing results of synthetic tests that investigate the dependence of lateral resolution on the station distribution and location of the seismic array relative to the earthquake epicentre. Synthetic seismograms are generated using a simple Ricker wavelet (Ricker 1953) with central frequency of 1.0 Hz. The arrival times of the wavelets are determined using a 1-D velocity model of the Earth (IASP91; Kennett & Engdahl 1991) for a given source location and specified seismic phases.

5.1 Distance and azimuth coverage

The lateral resolution of the backprojection method primarily depends on the distance and azimuthal coverage of the array of stations being used. We illustrate the effect of each criterion by generating synthetic seismograms for hypothetical arrays. To investigate the effect of distance coverage, we generate a synthetic array with stations at distances between 60° and 90° and at a fixed azimuth of 0° (Fig. 8a). The spacing between the stations is 0.1°, which leads to an array of 300 stations. The backprojection result from this array shows a circular arc of energy that passes through, and is maximum, at the input point source location (Fig. 8b). As expected, the good distance coverage of the array provides good constraints

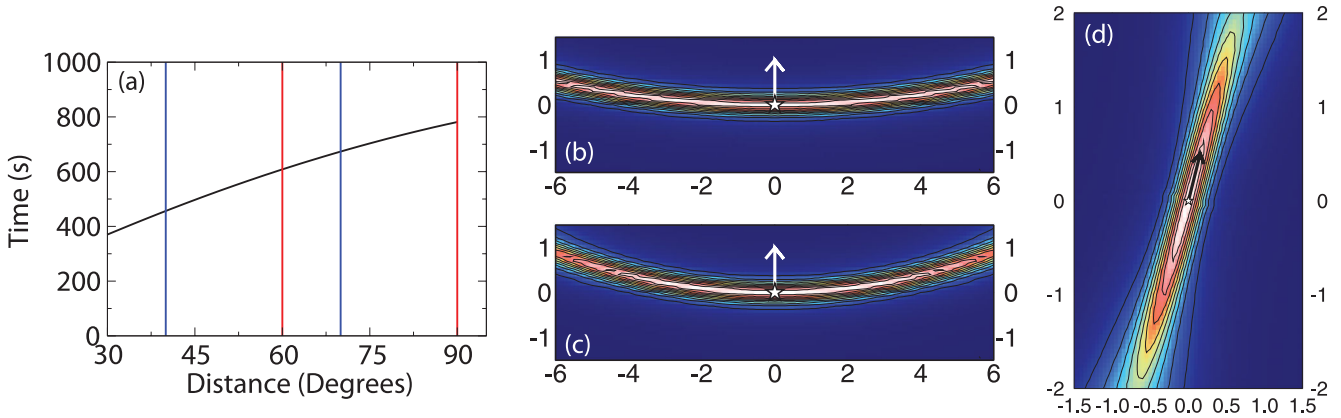

Figure 8. Effects of distance and azimuth coverage. (a) Synthetic arrays with stations at a range of distances, but all at the same azimuth are generated to determine the effect of poor azimuthal station coverage on backprojection results. This plot shows the range of distances used when generating the synthetic arrays on the traveltime curve (black line). The blue lines show the range for the 40°–70° array, and the red lines show the range for the 60°–90° array. These arrays each have 300 stations with a station spacing of 0.1°. (b) The backprojection result for a point source (white star) using the array with a distance range of 60°–90°. The colours represent the values of the integrated squared stacks from each gridpoint. White represents maximum energy and dark blue represents minimum energy. The white arrow is the direction to the array. The latitude/longitude tick marks are with respect to the point source (white star). (c) The same as (b) except using the array with a distance coverage of 40°–70°. (d) As with (b) and (c), this plot shows the backprojection result for a point source (white star). In this case, the synthetic array used has stations at a constant distance (75°) from the point source, but with an azimuthal coverage of 30°. The black arrow is the direction to the array.

on the distance of the point source from the array. Conversely, the lack of azimuthal coverage makes it difficult to constrain the azimuth of the point source. Fig. 8(c) shows that the resolution not only depends on the range of distances used, but also on the absolute distances of the stations. Here, a synthetic array is set up with the same distance range (30°), but it is closer to the epicentre (40°–70°; Fig. 8a). The backprojection result from this synthetic array shows that the recovered energy has a larger curvature and less lateral extent than in Fig. 8(b) (Fig. 8c). The improved lateral resolution for smaller absolute distances can be understood if one considers a *P*-wave traveltime curve (Fig. 8a). The *P*-wave slowness of closer arrays changes more, hence these arrays are more sensitive to changes in the source location. This dependence on slowness becomes even more important when considering distances at which core phases are the first to arrive. For example, the slowness of the core phase *PKIKP* is weakly dependent on distance (Fig. 2b), and is much less sensitive to changes in source location than the *P* phase.

A similar synthetic test with an array of stations at azimuths between 0° and 30°, a station spacing of 0.1°, and a constant distance of 75° is performed to investigate the effects of azimuthal coverage (Fig. 8d). The recovered energy using this array is now elongated in the direction of the array. This result shows that good azimuthal coverage of the array constrains the azimuth of the point source very well, and poor distance coverage leads to poor distance resolution in the direction of the array (Fig. 8d). For real seismic arrays, the shape and size of a resolution kernel are primarily controlled by the azimuthal and distance coverage, that is, the shape and size of the array. The synthetic tests also show that absolute distance affects the final result. These results illustrate limitations in using a single array for backprojection studies of source properties. One approach to improve resolution is to increase distance and azimuth coverage by using a global network of stations such as the Global Seismic Network (e.g. Walker *et al.* 2005; Walker & Shearer 2009; D'Amico *et al.* 2010). However, this data set presents its own challenges due to poor waveform coherence between the stations compared to that within a dense seismic array. Even when care is taken to group stations into subsets with similar waveforms, artefacts can still be an issue (Walker & Shearer 2009). In this study, we have attempted to take advantage of waveform coherence within a given array while improving station coverage by combining two arrays at different azimuths and distances.

5.2 Lateral resolution

As the earlier section demonstrates, lateral resolution using the backprojection method depends upon distance and azimuthal station coverage, and slowness of the phase used. By using only array data from Hi-net and TA, waveform similarity within the array is maintained, and both distance and azimuthal coverage are improved compared to a single array. In this section we evaluate how this approach improves resolution for the four regions considered in this study. Each of these regions present unique resolution issues due to their positions relative to Hi-net and TA. Therefore, synthetic tests will be presented separately for each region in subsequent subsections. For the sake of comparison, we arbitrarily choose the 70 per cent contour of maximum energy to interpret and compare the synthetic results. We estimate the minimum magnitude of an event above which rupture properties can be imaged using the area within the 70 per cent contour (Kanamori 1977).

5.2.1 Pisco, Peru

319 stations of the Transportable Array are distributed over a distance and azimuth range of 54°–75° and 321°–335°, respectively, relative to the epicentre of the 2007 August 15 M_w 8.0 Pisco, Peru, event (Fig. 9a). This distance range implies that the *P* phase is the first to arrive at these stations. On the other hand, the stations of the Hi-net array covers a distance and azimuth range of 133°–150° and 307°–323°, respectively. As discussed in the Data and Data Processing section (Section 3), a distance filter is applied to avoid complications due to the core-phase triplication. After applying the distance constraint, there are 138 stations with a clean *PKPbc* phase

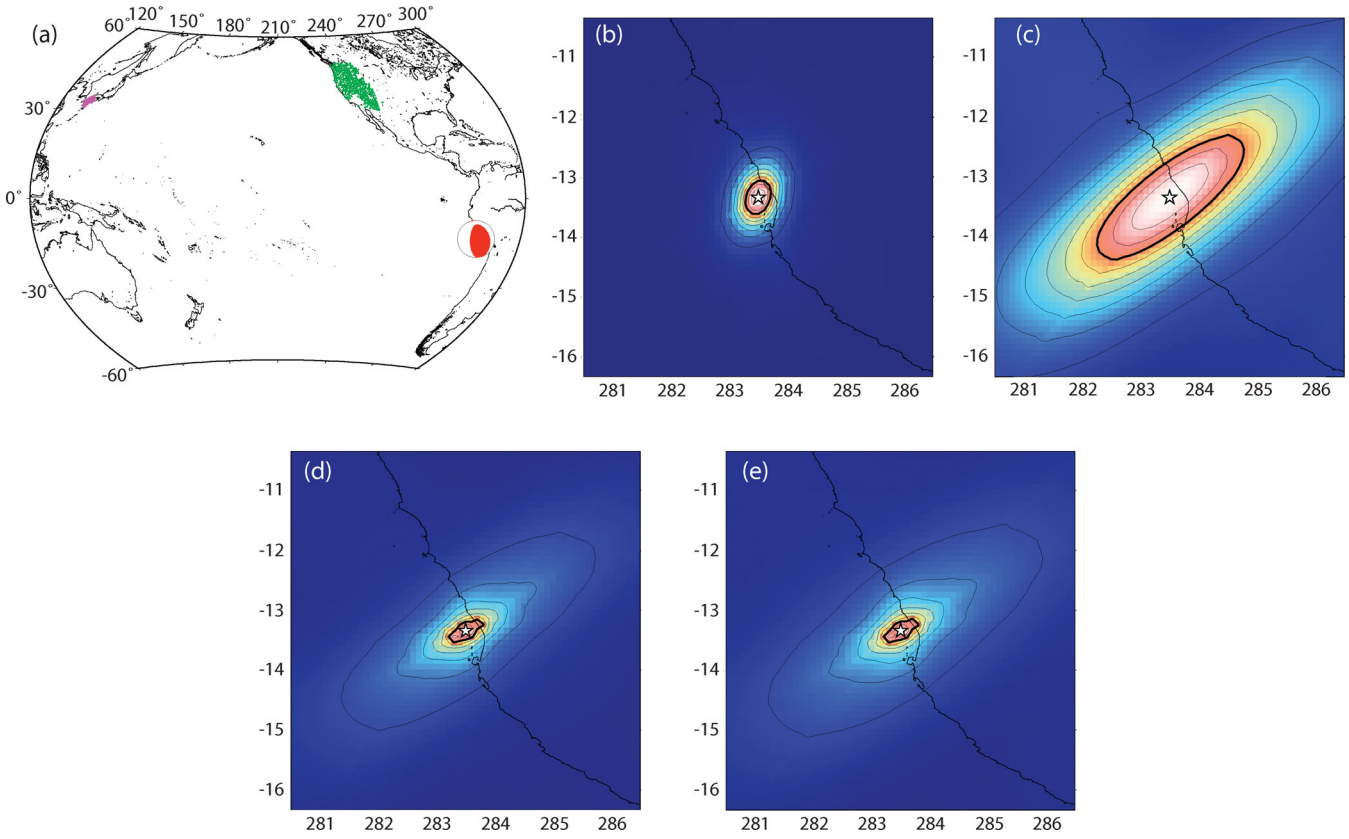

Figure 9. Peru synthetic tests. Backprojection results for a point source input at the hypocentre of the M_w 8.0 2007 Pisco, Peru, earthquake. (a) Distribution of stations from TA (green triangles) and Hi-net (pink triangles) with respect to the focal mechanism of the 2007 Peru event (Global CMT Catalogue; Dziewonski *et al.* 1981; Dziewonski & Woodhouse 1983). Note that there is a distance constraint of 146°–150° applied to the Hi-net data. (b) Backprojection result from a point source (white star) at the epicentre of the 2007 Peru event using synthetic TA data. White represents high energy release and dark blue represents low energy release. The light grey lines are the contours of maximum energy release in 10 per cent intervals. The black contour is the 70 per cent contour. The solid black line is the coastline. (c) The same as (b) except using synthetic Hi-net data. (d) The backprojection result when both synthetic TA and Hi-net data are combined. (e) The same as (d) except the core phases *PKIKP* and *PKPab* are included in the synthetic seismograms for Hi-net.

within a distance and azimuth range of 146°–150° and 309°–315°, respectively (Fig. 9a).

The recovered energy distribution using synthetic seismograms generated for TA and Hi-net from a point source are shown in Figs 9(b)–(e). By itself, the TA data images the point source very well (Fig. 9b). The area inside the 70 per cent contour is 2200 km^2. In contrast, the result using only Hi-net synthetic seismograms exhibits very poor resolution with an area of 30 000 km^2 inside the 70 per cent contour (Fig. 9c). The poor resolution using Hi-net is primarily a result of the poor azimuth and distance coverage of the array subset used in the analysis, as well as nearly constant slowness. Combining stacks from TA and Hi-net results in some improvement to the TA result (Fig. 9d). The 70 per cent contour area reduces to 1400 km^2, which corresponds to a moment magnitude of 7.1 using an empirical relationship between slip area and moment magnitude (Kanamori 1977). This threshold magnitude for imaging rupture properties is much lower than the magnitude of the Pisco, Peru, event (M_w 8.0), and therefore details of the rupture should be recoverable using the TA and Hi-net arrays. Finally, a synthetic test is performed including the core phases *PKPab* and *PKIKP* with the *PKPbc* phase in the synthetic seismograms for Hi-net stations to investigate the effects of other core phases not considered during stacking. As Fig. 9(e) shows, these additional phases cause only small changes on the final backprojection result due to the slowness differences between the core phases.

5.2.2 *Mentawai Islands*

The 2007 September 12 M_w 8.4 Mentawai Islands earthquake occurred at a distance and azimuth range of 45°–63° and 31°–40°, respectively, from Hi-net and 122°–141° and 28°–46°, respectively, from TA (Fig. S1a). For the 752 stations in Hi-net, the first phase to arrive is *P*, and for TA, there are 346 stations with *PKIKP* as the first arrival. The resolution kernel of a point source using Hi-net data has an area of 3900 km^2 inside the 70 per cent contour (Fig. S1b). In contrast, the area inside the 70 per cent contour using TA data is 87 000 km^2 (Fig. S1c). This poor resolution from the TA data is caused by the nearly constant slowness of the *PKIKP* phase (Fig. 2b). Combining the two arrays leads to an energy kernel with an area of 1700 km^2, with much better resolution in the dip direction than parallel to the trench (Fig. S1d). Therefore, the minimum earthquake magnitude that can be imaged is 7.2 (Kanamori 1977). In addition to imaging the M_w 8.4 event, this means that the data are also capable of imaging the rupture properties of the M_w 7.9 earthquake that occurred 12 hr after the M_w 8.4 event in the same region.

5.2.3 *Samoa Islands*

The epicentre of the 2009 September 29 M_w 8.1 Samoa Islands event is at a distance and azimuth range of 67°–75° and 310°–329°,

respectively, from Hi-net, and 71°–100° and 36°–60°, respectively, from TA (Fig. S2a). Therefore, the first phase to arrive for both Hi-net and TA is *P*. The number of stations in Hi-net and TA is 802 and 405, respectively. By itself, the TA data images the point source very well (Fig. S2b). The area inside the 70 per cent contour is 2300 km^2. The result using only Hi-net synthetic seismograms also exhibits good resolution with an area of 4700 km^2 inside the 70 per cent contour (Fig. S2c). In addition to being at *P* phase distances, the arrays also have good distance and azimuthal coverage, which leads to their small-resolution kernels. Better resolution using TA is due to the larger distance and azimuth range covered by TA compared to Hi-net. Combining stacks from TA and Hi-net results in a very small energy kernel with an area of 550 km^2 (Fig. S2d). Once again, using the empirical relationship of Kanamori (1977), the threshold moment magnitude associated with this region is 6.7, much less than the event magnitude on 2009 September 29.

5.2.4 Maule, Chile

The distance and azimuth range of the 390 TA stations from the epicentre of the 2010 February 27 M_w 8.8 Maule, Chile, earthquake is 67°–94° and 323°–353°, respectively. Therefore, the *P* phase is the first to arrive. The distance of stations used from Hi-net is limited to 155°° or greater to isolate the *PKIKP* phase. This results in a subset of 384 stations with a distance and azimuth range of 155°–162° and 263°–283°, respectively. The areas of the point source energy kernels for TA and Hi-net are 1700 km^2 and 50 000 km^2, respectively (Figs S3b and c). As with the Peru event, the limited distance coverage of Hi-net, as well as the slowness of the seismic phase being used, leads to its large resolution kernel. Combining stacks from both arrays leads to a slightly improved area of 1000 km^2 (Fig. S3d). The associated magnitude of this area is 7.0 (Kanamori 1977), therefore details of the M_w 8.8 earthquake can be imaged. Additional core phases are included in a final synthetic test to demonstrate that they do not affect the final backprojection results significantly (Fig. S3e).

6 CONCLUSIONS

The distribution of stations from TA and Hi-net provides good coverage to image the rupture details of five recent large earthquakes using the backprojection method. The spatio-temporal distribution of energy release from all five events shows that these ruptures are segmented into subevents with varying rupture directions and speeds. In some cases, gaps in the ruptures suggest that large earthquakes involve multiple fault segments that are triggered by slip on an adjacent segment. These rupture details are important for developing a better understanding of the tectonic parameters and conditions that control the size and dynamics of ruptures, and the seismic hazards associated with large earthquakes.

ACKNOWLEDGMENTS

The authors thank the National Research Institute for Earth Science and Disaster Prevention in Japan and the IRIS Data Management Center for making the Hi-net and TA data available. This manuscript benefitted from constructive reviews by Thomas Braun and Sebastian Rost. Some figures have been generated using the Generic Mapping Tools (Wessel & Smith 1991). This project was funded by NSF EAR-0609092.

REFERENCES

Allmann, B.P. & Shearer, P.M., 2007. A high-frequency secondary event during the 2004 Parkfield earthquake, *Science,* **318,** 1279–1283.

Baker, T., Granat, R. & Clayton, R.W., 2005. Real-time earthquake location using Kirchhoff reconstruction, *Bull. Seism. Soc. Am.,* **95,** 699–707.

Beavan, J., Wang, X., Holden, C., Wilson, K., Power, W., Prasetya, G., Bevis, M. & Kautoke, R., 2010. Near-simultaneous great earthquakes at Tongan megathrust and outer rise in September 2009, *Nature,* **466,** 959–963.

Biggs, J., Robinson, D.P. & Dixon, T.H., 2009. The 2007 Pisco, Peru, earthquake (Mw8.0): seismology and geodesy, *Geophys. J. Int.,* **176,** 657–669.

Chlieh, M., Avouac, J.P., Sieh, K., Natawidjaja, D.H. & Galetzka, J., 2008. Heterogeneous coupling of the Sumatran megathrust constrained by geodetic and paleogeodetic measurements, *J. geophys. Res.,* **113,** B05305, doi:10.1029/2007JB004981.

D'Amico, S., Koper, K.D., Herrmann, R.B., Akinci, A. & Malagnini, L., 2010. Imaging the rupture of the M_w 6.3 April 6, 2009 L'Aquila, Italy earthquake using back-projection of teleseismic P-waves, *Geophys. Res. Lett.,* **37,** L03301, doi:10.1029/2009GL042156.

Delouis, B., Nocquet, J.-M. & Vallee, M., 2010. Slip distribution of the February 27, 2010 Mw = 8.8 Maule Earthquake, central Chile, from static and high-rate GPS, InSAR, and broadband teleseismic data, *Geophys. Res. Lett.,* **37,** L17305, doi:10.1029/2010GL043899.

Dziewonski, A.M. & Woodhouse, J.H., 1983. An experiment in systematic study of global seismicity: centroid-moment tensor solutions for 201 moderate and large earthquakes of 1981, *J. geophys. Res.,* **88,** 3247–3271.

Dziewonski, A.M., Chou, T.A. & Woodhouse, J.H., 1981. Determination of earthquake source parameters from waveform data for studies of global and regional seismicity, *J. geophys. Res.,* **86,** 2825–2852.

Ekström, G., Nettles, M. & Abers, G., 2003. Glacial earthquakes, *Science,* **302,** 622–624.

Fritz, H.M., Kalligeris, N., Borrero, J.C., Broncano, P. & Ortega, E., 2008. The 15 August 2007 Peru tsunami runup observations and modeling, *Geophys. Res. Lett.,* **35,** L10604, doi:10.1029/2008GL033494.

Fromm, R., Alvarado, P., Beck, S.L. & Zandt, G., 2006. The April 9, 2001 Juan Fernandez Ridge (Mw 6.7) tensional outer-rise earthquake and its aftershock sequence, *J. Seism.,* **10,** 163–170.

Habermann, R.E. & Wyss, M., 1984. Earthquake triggering during preparation for great earthquakes, *Geophys. Res. Lett.,* **11,** 291–294.

Hébert, H., Reymond, D., Krien, Y., Vergoz, J., Schindelé, F., Roger, J. & Loevenbruck, A., 2009. The 15 August 2007 Peru earthquake and tsunami: influence of the Source Characteristics on the Tsunami Heights, *Pure Appl. Geophys.,* **166,** 211–232.

Heuret, A., Lallemand, S., Funiciello, F., Piromallo, C. & Faccenna, C., 2011. Physical characteristics of subduction interface type seismogenic zones revisited, *Geochem. Geophys. Geosyst.,* **12,** Q01004, doi:10.1029/2010GC003230.

Hino, R. *et al.*, 2009. Insight into complex rupturing of the immature bending normal fault in the outer slope of the Japan Trench from aftershocks of the 2005 Sanriku earthquake (Mw = 7.0) located by ocean bottom seismometry, *Geochem. Geophys. Geosyst.,* **10,** Q07O18, doi:10.1029/2009GC002415.

Honda, R. & Shin, A., 2009. Array back-projection imaging of the 2007 Niigataken Chuetsu-oki earthquake striking the world's largest nuclear power plant, *Bull. seism. Soc. Am.,* **99,** 141–147.

von Huene, R., Corvalan, J., Flueh, E.R., Hinz, K., Korstgard, J., Ranero, C.R. & Weinrebe, W., 1997. Tectonic control of the subducting Juan Fernández Ridge on the Andean margin near Valparaiso, Chile, *Tectonics,* **16,** 474–488.

Ishii, M., Shearer, P.M., Houston, H. & Vidale, J.E., 2005. Extent, duration and speed of the 2004 Sumatra-Andaman earthquake imaged by the Hi-net array, *Nature,* **435,** 933–936.

Ishii, M., Shearer, P.M., Houston, H. & Vidale, J.E., 2007. Teleseismic P wave imaging of the 26 December 2004 Sumatra-Andaman and 28 March 2005 Sumatra earthquake ruptures using the Hi-Net array, *J. geophys. Res.,* **112,** B11307, doi:10.1029/2006JB004700.

Kanamori, H., 1972. Mechanism of tsunami earthquakes, *Phys. Earth Planet. Inter.,* **6,** 346–359.
Kanamori, H., 1977. The energy release in great earthquakes, *J. geophys. Res.,* **82,** 2981–2987.
Kao, H. & Shan, S.-J., 2004. The source-scanning algorithm: mapping the distribution of seismic sources in time and space, *Geophys. J. Int.,* **157,** 589–594.
Kao, H. & Shan, S.-J., 2007. Rapid identification of earthquake rupture plane using Source-Scanning Algorithms, *Geophys. J. Int.,* **168,** 1011–1020.
Kato, N. & Seno, T., 2003. Hypocenter depths of large interplate earthquakes and their relation to seismic coupling, *Earth Planet. Sci. Lett.,* **210,** 53–63.
Kennett, B.L.N. & Engdahl, E.R., 1991. Traveltimes for global earthquake location and phase identification, *Geophys. J. Int.,* **105,** 429–465.
Kiser, E. & Ishii, M., 2011. The 2010 Mw 8.8 Chile earthquake: triggering on multiple segments and frequency-dependent rupture behavior, *Geophys. Res. Lett.,* **38,** doi:10.1029/2011GL047140.
Kiser, E., Ishii, M., Langmuir, C.H., Shearer, P.M. & Hirose, H., 2011, Insights into the mechanism of intermediate-depth earthquakes from source properties as imaged by back-projection of multiple seismic phases, *J. geophys. Res.,* **116,** doi:10.1029/2010JB007831.
Konca, A.O. *et al.*, 2008. Partial rupture of a locked patch of the Sumatra megathrust during the 2007 earthquake sequence, *Nature,* **456,** 631–635.
Krüeger, F. & Ohrnberger, M., 2005. Tracking the rupture of the Mw = 9.3 Sumatra earthquake over 1,150 km at teleseismic distance, *Nature,* **435,** 937–939.
Lay, T., Ammon, C.J., Hutko, A.R. & Kanamori, H., 2010a. Effects of kinematic constraints on teleseismic finite-source rupture inversion: Great Peruvian earthquakes of 23 June 2001 and 15 August 2007, *Bull. seism. Soc. Am.,* **100,** 969–994.
Lay, T., Ammon, C.J., Kanamori, H., Koper, K.D., Sufri, O. & Hutko, A.R., 2010b. Teleseismic inversion for rupture process of the 27 February 2010 Chile (Mw 8.8) earthquake, *Geophys. Res. Lett.,* **37,** L13301, doi:10.1029/2010GL043379.
Lay, T., Ammon, C.J., Kanamori, H., Rivera, L., Koper, K.D. & Hutko, A.R., 2010c. The 2009 Samoa-Tonga great earthquake triggered doublet, *Nature,* **466,** 964–968.
Lorito, S. *et al.*, 2011. Limited overlap between the seismic gap and coseismic slip of the great 2010 Chile earthquake, *Nature Geosci.,* **4,** 173–177.
MacAyeal, D.R. *et al.*, 2006. Transoceanic wave propagation links iceberg calving margins of Antarctica with storms in tropics and northern hemisphere, *Geophys. Res. Lett.,* **33,** L17502, doi:10.1029/2006GL027235.
Madariaga, R., 1977. High-frequency radiation from crack (stress drop) models of earthquake faulting, *Geophys. J. R. astr. Soc.,* **51,** 625–651.
Masson, D.G., 1991. Fault patterns at outer trench walls, *Mar. geophys. Res.,* **13,** 209–225.
McMechan, G.A., Luetgert, J.H. & Mooney, W.D., 1985. Imaging of earthquake sources in Long Valley caldera, California, 1983, *Bull. seism. Soc. Am.,* **75,** 1005–1020.
Meng, L., Inbal, A. & Ampuero, J.-P., 2011. A window into the complexity of the dynamic rupture of the 2011 Mw 9 Tohoku-Oki earthquake, *Geophys. Res. Lett.,* **38,** doi:10.1029/2011GL048118.
Moreno, M., Rosenau, M. & Oncken, O., 2010. Maule earthquake slip correlates with pre-seismic locking of Andean subduction zone, *Nature,* **467,** 198–202.
Motagh, M., Wang, R., Walter, T.R., Buergmann, R., Fielding, E., Anderssohn, J. & Zschau, J., 2008. Coseismic slip model of the 2007 August Pisco earthquake (Peru) as constrained by wide swath radar observations, *Geophys. J. Int.,* **174,** 842–848.
Nelson, P., Shin, A. & Hiroyuki, F., 2008. Rupture process of the 2007 Notohanto earthquake by using an isochrones back-projection method and K-NET/KiK-net data, *Earth Planets Space,* **60,** 1035–1040.
Obara, K., Kasahara, K., Hori, S. & Okada, Y., 2005. A densely distributed high-sensitivity seismograph network in Japan: Hi-net by National Research Institute for Earth Science and Disaster Prevention, *Rev. Sci. Instrum.,* **76,** 021301, doi:10.1063/1.1854197.
Okada, Y., Kasahara, K., Hori, S., Obara, K., Sekiguchi, S., Fujiwara, H. & Yamamoto, A., 2004. Recent progress of seismic observation networks in Japan: Hi-net, F-net, K-NET and KiK-net, *Earth Planets Space,* **56,** xv–xxviii.
Okal, E.A. *et al.*, 2010. Field survey of the Samoa tsunami of 29 September 2009, *Seis. Res. Lett.,* **81,** 577–591.
Perfettini, H. *et al.*, 2010. Seismic and aseismic slip on the central Peru megathrust, *Nature,* **465,** 78–81.
Pritchard, M.E. & Fielding, E.J., 2008. A study of the 2006 and 2007 earthquake sequence of Pisco, Peru, with InSAR and teleseismic data, *Geophys. Res. Lett.,* **35,** L09308, doi:10.1029/2008GL033374.
Rietbrock, A. & Scherbaum, F., 1994. Acoustic imaging of earthquake sources from the Chalfant Valley, 1985. aftershock series, *Geophys. J. Int.,* **119,** 260–268.
Ricker, N., 1953. The form and laws of propagation of seismic wavelets, *Geophysics,* **18,** 10–40.
Sibson, R.H., 1982. Fault zone models, heat flow, and the depth distribution of earthquakes in the continental crust of the United States, *Bull. seism. Soc. Am.,* **72,** 151–163.
Sladen, A. *et al.*, 2010. Source model of the 2007 Mw 8.0 Pisco, Peru earthquake: implications for seismogenic behavior of subduction megathrusts, *J. geophys. Res.,* **115,** B02405, doi:10.1029/2009JB006429.
Walker, K. & Shearer, P.M., 2009. Illuminating the near-sonic rupture velocities of the intracontinental Kokoxili Mw 7.8 and Denali Mw 7.9 strike-slip earthquakes with global P-wave back projection imaging, *J. geophys. Res.,* **114,** B02304, doi:10.1029/2008JB005738.
Walker, K., Ishii, M. & Shearer, P.M., 2005. Rupture details of the 28 March 2005 Sumatra Mw 8.6 earthquake imaged with teleseismic *P* waves, *Geophys. Res. Lett.,* **32,** L24303, doi:10.1029/2005GL024395.
Wessel, P. & Smith, W.H. F., 1991. Free software helps map and display data, *EOS, Trans. Am. geophys. Un.,* **72,** 441.
Xu, Y., Koper, K.D., Sufri, O., Zhu, L. & Hutko, A.R., 2009. Rupture imaging of the Mw 7.9 12 May 2008 Wenchuan earthquake from back projection of teleseismic *P* waves, *Geochem. Geophys. Geosyst.,* **10,** Q04006, doi:10.1029/2008GC002335.

SUPPORTING INFORMATION

Additional Supporting Information may be found in the online version of this article:

Figure S1. Mentawai Islands synthetic tests. Backprojection results for a point source at the epicentre of the M_w 8.4 2007 Mentawai Islands earthquake using synthetic data from both TA and Hi-net. (a) Distribution of stations from TA (green triangles) and Hi-net (pink triangles) with respect to the the focal mechanism of the 2007 Mentawai Islands event (Global CMT Catalogue; Dziewonski *et al.* 1981; Dziewonski & Woodhouse 1983). (b) Backprojection result from a point source (white star) at the epicentre of the 2007 Mentawai Islands event using Hi-net synthetic data. The symbols are the same as in Fig. 9. (c) The same as (b) except using TA synthetic data. (d) The backprojection result when both Hi-net and TA synthetic data are used.
Figure S2. Samoa Islands synthetic tests. Backprojection results for a point source at the epicentre of the M_w 8.1 2009 Samoa Islands earthquake using synthetic data from both TA and Hi-net. (a) Distribution of stations from TA (green triangles) and Hi-net (pink triangles) with respect to the the focal mechanism of the 2009 Samoa Islands event (Global CMT Catalogue; Dziewonski *et al.* 1981; Dziewonski & Woodhouse 1983). (b) Backprojection result from a point source (white star) at the epicentre of the 2009 Samoa Islands event using TA synthetic data. The symbols are the same as in Fig. 9. (c) The same as (b) except using Hi-net synthetic data. (d) The backprojection result when both TA and Hi-net synthetic data are used.
Figure S3. Maule, Chile, synthetic tests. Backprojection results for a point source at the epicentre of the M_w 8.8 2010 Maule,

Chile, earthquake using synthetic data from both TA and Hi-net. (a) Distribution of stations from TA (green triangles) and Hi-net (pink triangles) with respect to the the focal mechanism of the 2010 Chile event (Global CMT Catalogue; Dziewonski *et al.* 1981; Dziewonski & Woodhouse 1983). (b) Backprojection result from a point source (white star) at the epicentre of the 2010 Chile event using TA synthetic data. The symbols are the same as in Fig. 9. (c) The same as (b) except using Hi-net synthetic data. (d) The backprojection result when both TA and Hi-net synthetic data are used. (e) The same as (d) except the core phases *PKPab* and *PKPbc* are included in the synthetic seismograms from Hi-net.

Movie S1. The 2009 September 29 Samoa Islands earthquake. Backprojection results for the 2009 Samoa Islands earthquake. The white line is the coastline. The black star is the epicentre. Dark red colours show regions of high energy release and dark blue colours show regions of low energy release.

Movie S2. The 2010 February 27 Maule, Chile, earthquake. Backprojection results for the 2010 Chile earthquake using both Hi-net and TA data. The symbols are the same as in Movie S1.

Movie S3. 2010 Maule, Chile, earthquake: TA data only. Backprojection results for the 2010 Chile earthquake using only TA data. The symbols are the same as in Movie S1.